Energy Advances

ROYAL SOCIETY OF CHEMISTRY

PAPER

View Article Online
View Journal | View Issue

Check for updates

Cite this: *Energy Adv.*, 2023, 2, 1650

High-performance asymmetric supercapacitor device with nickel–cobalt bimetallic sites encapsulated in multilayered nanotubes†

Rahul Patil, ‡[a] Lingaraj Pradhan,‡[bc] Babasaheb M. Matsagar,[d] Omnarayan Agrawal,[a] Kevin C.-W. Wu,[de] Bikash Kumar Jena*[bc] and Saikat Dutta*[a]

Received 13th May 2023,
Accepted 10th August 2023

DOI: 10.1039/d3ya00206c

rsc.li/energy-advances

Enhanced faradaic capacitance can be achieved by using a metallic heterostructure as a result of the intrinsic activity of the electrodes. Optimizing the multimetallic heterostructure is key to improving the intrinsic activity of the electrodes. Herein, a consolidated strategy of a multimetallic design with predominantly nickel, cobalt, and zinc centers on multiwalled nanotubes was developed *via* pyrolysis of a trimetallic metal–organic framework at 800 °C. The resulting C-ZIF-800 material offers a multiwalled nanotube-like structure that facilitates the encapsulation of multimetallic sites with predominantly nickel and cobalt centers on a nanotube-like N–C interface. XRD, HRTEM, XPS, and EXAFS spectroscopic analysis support the metallic valence state of the Ni and Co centers encapsulated in the N–C nanotubes. C-ZIF-800 offers an outstanding specific capacitance of 849.47 F g^{-1} at a current density of 1 A g^{-1}. Based on three-electrode electrochemical measurements, an asymmetric supercapacitor (ASC) device (C-ZIF-800//AC) was fabricated with a wide potential window of 1.7 V. The device offers an excellent specific capacity of 599.7 C g^{-1} at 0.25 A g^{-1} with an exceptional energy density of 141.59 W h kg^{-1} at a power density of 212.5 W kg^{-1}, and remaining 4250 W kg^{-1} after retaining 81.93 W h kg^{-1} of energy density. The as-fabricated device demonstrated its excellent potential for future energy storage applications by illuminating a red LED light for 60 min by combining two devices in series.

Open Access Article. Published on 10 agosto 2023. Downloaded on 28/07/2025 11:14:35.
This article is licensed under a Creative Commons Attribution 3.0 Unported Licence.

Introduction

Wide-voltage aqueous asymmetric supercapacitors (ASCs) break the energy storage restrictions of symmetric cells while offering promising future electronic systems with high energy-power density and cycle life due to their facile fabrication, operational safety, and high ionic conductivity.[1,2] Unidirectional charging in ASCs, however, depends on the coupling of a carbon molecular sieve with ordered mesoporous carbon, which can act as a capacitive analog of semiconductor-based diodes.[3] Using two different electrodes, ASCs can expand the window of operating voltage beyond the thermodynamic decomposition voltage of electrolytes by enhancing the energy storage capacity of symmetric systems.[4] To the hierarchical architecture and high surface area are attributed the greater cycling safety and effective electrochemical performance with high specific capacitance and highest capacity retention by porous bilayers of $NiZn(CO_3)(OH)_2$–$Ni_2(CO_3)(OH)_2$ on Ni foam.[5,6] NiO/Ni-MOF ASCs exhibit an energy density of 31.3 W h kg^{-1} for cyclic stability with capacitance retention of 88.7% over 2000 cycles.[7] Nitrogen-doped graphene has been used as a host to encapsulate metal nanoparticles, such as nickel–cobalt nitride, as a core–shell structure for flexible solid-state ASC devices with exceptional power density.[8] The structure–property correlations of metal–organic-framework-derived superstructure materials help in an exploration of their potential as supercapacitors and capacitive-deionization electrodes.[9,10] Capacitance-dependent supercapacitors with a transformative improvement in performance require high energy density and a graphitic-type structure with metal loading.[11] Differentiation between double-layer and pseudocapacitive charge storage forms the basis of

[a] *Electrochemical Energy & Sensor Research Laboratory, Amity Institute of Click Chemistry Research & Studies, Amity University Noida, India. E-mail: sdutta2@amity.edu*
[b] *Materials Chemistry Department, CSIR-Institute of Minerals and Materials Technology, Bhubaneswar-751013, India*
[c] *Academy of Scientific and Innovative Research (AcSIR), Ghaziabad 201002, India. E-mail: bikash@immt.res.in*
[d] *Department of Chemical Engineering, National Taiwan University, No. 1, Sec. 4, Roosevelt Road, Taipei 10617, Taiwan*
[e] *Department of Chemical Engineering and Materials Science, Yuan Ze University, Chung-Li, Taoyuan, Taiwan*

† Electronic supplementary information (ESI) available. See DOI: https://doi.org/10.1039/d3ya00206c

‡ Both the authors contributed equally.

© 2023 The Author(s). Published by the Royal Society of Chemistry

Open Access Article. Published on 10 agosto 2023. Downloaded on 28/07/2025 11:14:35.
This article is licensed under a Creative Commons Attribution 3.0 Unported Licence.

non-faradaic surface-controlled kinetics. In contrast, pseudocapacitive to battery-type charge storage is called the faradaic process, which runs on diffusion-controlled kinetics.[12] Combining faradaic reactions and capacitive electrode charging not only for a monovalent cation or anion, but for use in an ASC is an evolutionary step for enhanced capacitance.[12] The capacitance of the electrochemical interface is separated into faradaic pseudocapacitance and non-faradaic double-layer capacitance; however, faradaic intercalation depends on confinement by the microenvironment.[13] Ni-based pseudocapacitive electrode materials remain challenging owing to their weak electrical conductivity, resulting in large volume expansion during repeated intercalation/deintercalation processes.[14] Higher specific capacitance and nearly ideal capacitive behavior in aqueous electrolytes render electrode materials for high-power charge storage with the electrochemical capacitance of both faradaic and non-faradaic types for clarifying the capacitive mechanism.[15] Full exposure of metal sites in the faradaic reaction with excellent pseudocapacitance performance, such as Ni-NOG-1.5 with a gravimetry capacitance of 532 F g^{-1} at a current density of 1 A g^{-1} with an ASC assembled with Ni-NOG-1.5 and activated carbon considered as the negative electrode.[16] A low capacitive anode material significantly affects the performance of an ASC, wherein low-electrical conductivity limits capacitive energy storage.[2,17–19] The accelerated ion diffusion and charge mobility support an enhanced specific capacitance and cycle stability to provide an ultrahigh energy density by introducing abundant oxygen vacancies.[20] This extends to an adaptive pore structure for capacitive electrode materials to achieve ultrahigh energy density.[21]

Integrated carbon nanotubes (CNTs) and nickel–cobalt–phosphate (NiCo–P) offer a maximum capacitance retention rate of 86% with excellent energy density in an ASC with 92.4% retention of capacitance upon 10 000 charge–discharge cycles.[22] The transition of the NF/MnP/NiCoP composite occurs in different charge/discharge cycles wherein the specific capacitance was enhanced with extended charge/discharge cycles.[23] The Co/Ni ratio significantly affects the gravimetry capacitance of the $Ni_{4-x}Co_xWO_4$/HPC electrode. The $Ni_3Co_1WO_4$/HPC electrode offers an excellent gravimetry capacitance of 1084 F g^{-1} (364.5 C g^{-1}) at a current density of 0.5 A g^{-1} in 6 M KOH due to a unique nanostructure with synergistic effects between nickel and cobalt ions.[24] The nickel–cobalt phosphate clustered nanoparticle offers pseudocapacitive behavior with a maximum specific capacitance of 2228 F g^{-1} (891 C g^{-1}) at 1.5 A g^{-1}. Moreover, an aqueous hybrid asymmetric supercapacitor (AHAS) device exhibits a higher specific capacitance of 185 F g^{-1} with an energy density of 65.7 W h kg^{-1} at 2.2 kW kg^{-1} power density with capacitance retention of 97%.[25] Towards enhanced capacitance, three-dimensional structured diatoms $MnFeO_x$ composed of MnO with FeOOH nanorods exhibited high capacitance.[26] Similarly, FeOOH/PPy on a diatomic ternary complex was assembled to form oxygen vacancies and mesopores for enhanced supercapacitor features.[27] Consequently, phosphorus vacancies regulate the interfacial coupling of a biotemplated CoP@FeP_2 heterostructure with boosted pseudocapacitive

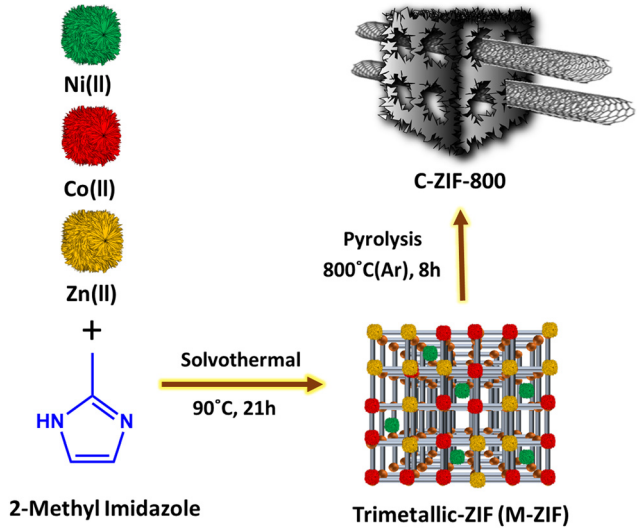

Scheme 1 Illustration of the solvothermal treatment of M-ZIF followed by pyrolysis at 800 °C under argon.

kinetics for ASCs with a high energy density of 45.5 W h kg^{-1} at a high power density *via* defect regulation.[28] Similar co-regulation of 3D cobalt phosphide in a vanadium-doped V-CoP_x hierarchical heteroatomic electrode exhibited excellent energy density and cyclic stability.[29] NiO also plays a major role in enhancing pseudocapacitance.[30] Ternary nanocomposites also play a significant role in supercapacitor electrodes.[31,32]

Herein, we describe a strategy for deriving an Ni and Co metal encapsulated N–C porous matrix of C-ZIF-800 from M-ZIF *via* thermal pyrolysis at 800 °C. C-ZIF-800 contains a multi-walled carbon nanotube shell of several hundred nanometers in length. It offers predominant Ni and Co sites due to the thermal pyrolysis-driven reduction of M^{2+} to M (Ni, Co) (Scheme 1). C-ZIF-800 was extensively characterized by surface spectroscopy (XPS, XAS, Raman) and transmission electron microscopy (HR-TEM) with high-resolution techniques confirming the presence of an MWCNT-like morphology with encapsulated Ni and Co sites. A pseudocapacitor-type electrode, which further demonstrates the charge–discharge mechanism, follows faradaic behavior by using C-ZIF-800. The ASC performance was tested in an asymmetric coin cell (CR2032) wherein activated carbon (AC) acts as an anode and C-ZIF-800 as a cathode, to light a 1.5 V LED with extremely high brightness for about 60 minutes.

The PXRD patterns of C-ZIF-700 to 800 samples exhibit three significant peaks at 2θ 45, 52, 76 corresponding to metallic nickel intensity for the (111), (200), and (220) planes (Fig. 1(a)). The XRD of M-ZIF resembles a few similar planes of ZIF-8[33] and ZIF-67,[34] conforming to a stable trimetallic framework (Fig. S1, ESI†). The BET surface area measured by N_2 sorption (Fig. 1(b)) for C-ZIF-800 exhibits a surface area of 208.28 m^2 g^{-1}. C-ZIF-800 shows a type-IV isotherm, including a hysteresis loop with adsorption–desorption of mesopores at higher P/P_0, suggesting the presence of mesopores. The pore distribution of C-ZIF-800 (Fig. 1(c)) was confirmed on the basis of a Barrett–Joyner–Halenda

Open Access Article. Published on 10 agosto 2023. Downloaded on 28/07/2025 11:14:35.
This article is licensed under a Creative Commons Attribution 3.0 Unported Licence.

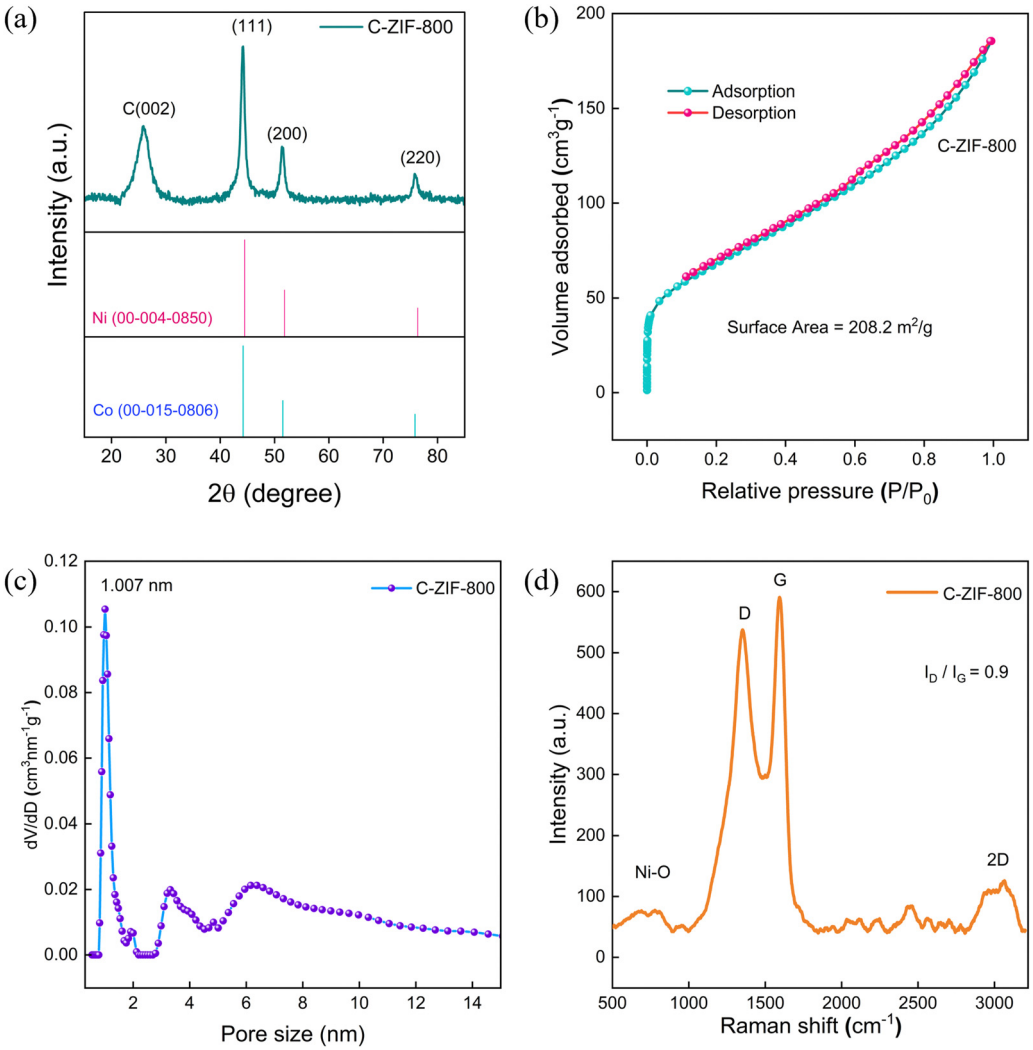

Fig. 1 (a) PXRD patterns of C-ZIF-800. (b) N_2 sorption isotherm of C-ZIF-800. (c) BHJ pore size distributions of C-ZIF-800. (d) Raman scattering spectrum of C-ZIF-800.

(BJH) model showing an identical pore width (1 nm) in the micropore region, including mesoporosity with a peak for pore dimensions of 3–10 nm. C-ZIF-800 was further confirmed from the Raman scattering spectrum (Fig. 1(d)) in which the D, G, and 2D bands appeared. The I_D/I_G ratio was found to be 0.90, confirming high graphitic degree in the material. Additionally, peaks at 520 cm^{-1} correspond to crystalline Ni–O lattice[35] vibrations in the C-ZIF-800 sample. Combining XRD and Raman analysis, the predominant Ni-sites consist of crystalline Ni nanoparticles and Ni–oxide in C-ZIF-800.

The deconvoluted spectral plots of the high-resolution X-ray photoelectron spectra (HR-XPS) of Ni 2p show a major peak at 854.7 eV (Fig. 2(a)), representing the formation of Ni–OH/Ni-O. Similarly, the Co $2p_{3/2}$ peak at 778.4 eV corresponds to metallic Co, along with peaks at 780.4 eV and 783.5 eV corresponding to CoO_x/CoC_xN_y and CoN_y (Fig. 2(b)). The Zn 2p spectra suggest the formation of Zn–O (~1022 eV) (Fig. S2(a), ESI†). The deconvolution plot of N 1s (Fig. 2(c)) confirms the presence of pyridinic, pyrrolic, and oxidized N. Deconvolution of C 1s indicates three peaks associated with C–C/C═C at 284.7 eV, C–N/C–OH at 285.6 eV; and C(O)–O at 289.08 eV (Fig. S2(b), ESI†). Moreover, O 1s peaks are associated with –C═O at 531.7 eV and C–O at 533.1 eV (Fig. S2(c), ESI†). The survey spectra of C-ZIF-800 are presented in Fig. 2(d)) along with the elemental composition of each element in C-ZIF-800. The oxidation state of Ni species in C-ZIF-800 was further investigated with electron paramagnetic resonance (EPR) spectroscopy (Fig. 2(e)) at room temperature (298 K) with g value 2.28 assigned to an unpaired electron in the $3d_{x^2-y^2}$ orbital of Ni(II). The Fourier transformation of the phase-corrected extended X-ray absorption fine structure (EXAFS) spectra shows a peak at 2.10 Å (Fig. 2(f)) corresponding to an Ni–Ni interaction similar to Ni foil. Moreover, the broad region in the *R*-space curve at ~1.5 Å suggests the formation of Ni–O. The XAS spectra of C-ZIF-800 contain relative intensities and edge positions (Fig. S5, ESI†) at 8334 eV, corresponding to a 3d and 4p orbital hybridization of Ni followed by a peak at 8340 eV before multiple scattering peaks above 8350 eV. Moreover, the energy absorption curve suggests a higher fraction of Ni–O bonds (Fig. S5, ESI†), which indicates the partially oxidized state of the Ni species in C-ZIF-800.

© 2023 The Author(s). Published by the Royal Society of Chemistry

Open Access Article. Published on 10 agosto 2023. Downloaded on 28/07/2025 11:14:35.
This article is licensed under a Creative Commons Attribution 3.0 Unported Licence.

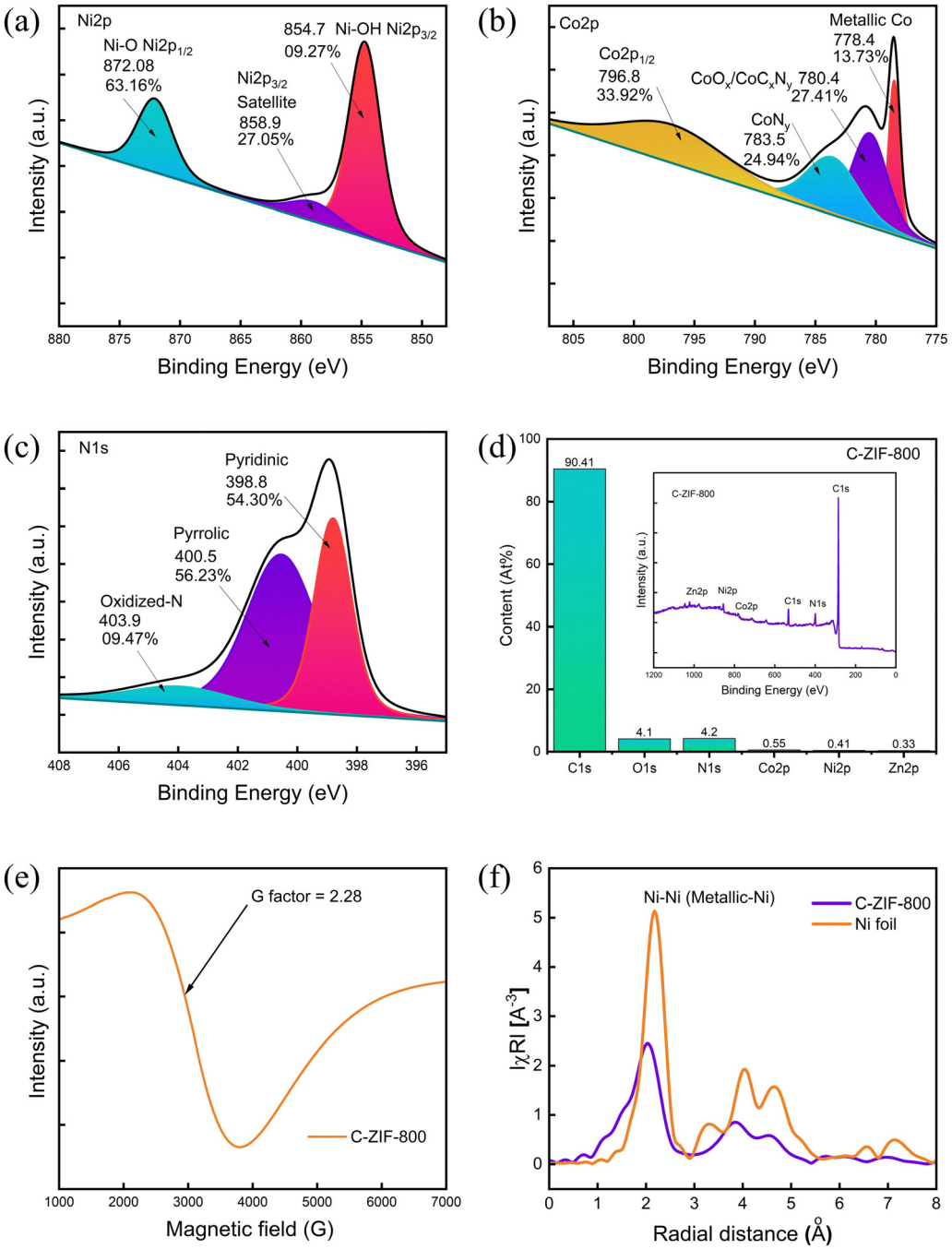

Fig. 2 XPS spectra for C-ZIF-800: (a) deconvoluted Ni 2p spectrum with Ni $2p_{3/2}$ peak, (b) deconvoluted Co 2p, and (c) N 1s. (d) Elemental content of C-ZIF-800 from XPS. (e) EPR spectra of C-ZIF-800 at 298 K. (f) FT-EXAFS spectra in *R*-space for Ni foil and C-ZIF-800.

Field-emission scanning electron microscopy (FE-SEM) of C-ZIF-700 and C-ZIF-800 reveals rectangular-shaped particles like that of the parent M-ZIF, resulting in a fused layered topology with a porous surface (Fig. 3(a) and (b)). The porosity level was further increased with the temperature of pyrolysis (800 °C) resulting in C-ZIF-800 with no major change in overall morphology (Fig. 3(b)). The porous architecture of C-ZIF-700, as found in the SEM images, is consistent with the porosity profile from the BJH pore profile (Fig. 1(c)). Transmission electron microscopy (TEM) analysis of C-ZIF-700 showed a multi-wall carbon layer containing a tube-like morphology (Fig. 3(c)) which holds Ni sites in encapsulated form (Fig. 3(d)). An increase in carbon nanotube volume is expected to increase at higher pyrolysis temperatures by a hard-templating effect of ZnO. The formation of the highly porous architecture of C-ZIF-800 offers a multiwalled nanotube morphology, which is enhanced at a higher pyrolysis temperature of 800 °C. Therefore, hard templating by ZnO supports the formation of an MWCNT architecture longer than 100 nm (Fig. 3(e) and (f)), in which continuous multiwalled tube-like growth is evident. A connection between MWCNT and double-layer capacitance can be assumed based on the experimental results for electrochemical impedance and

Open Access Article. Published on 10 agosto 2023. Downloaded on 28/07/2025 11:14:35.
This article is licensed under a Creative Commons Attribution 3.0 Unported Licence.

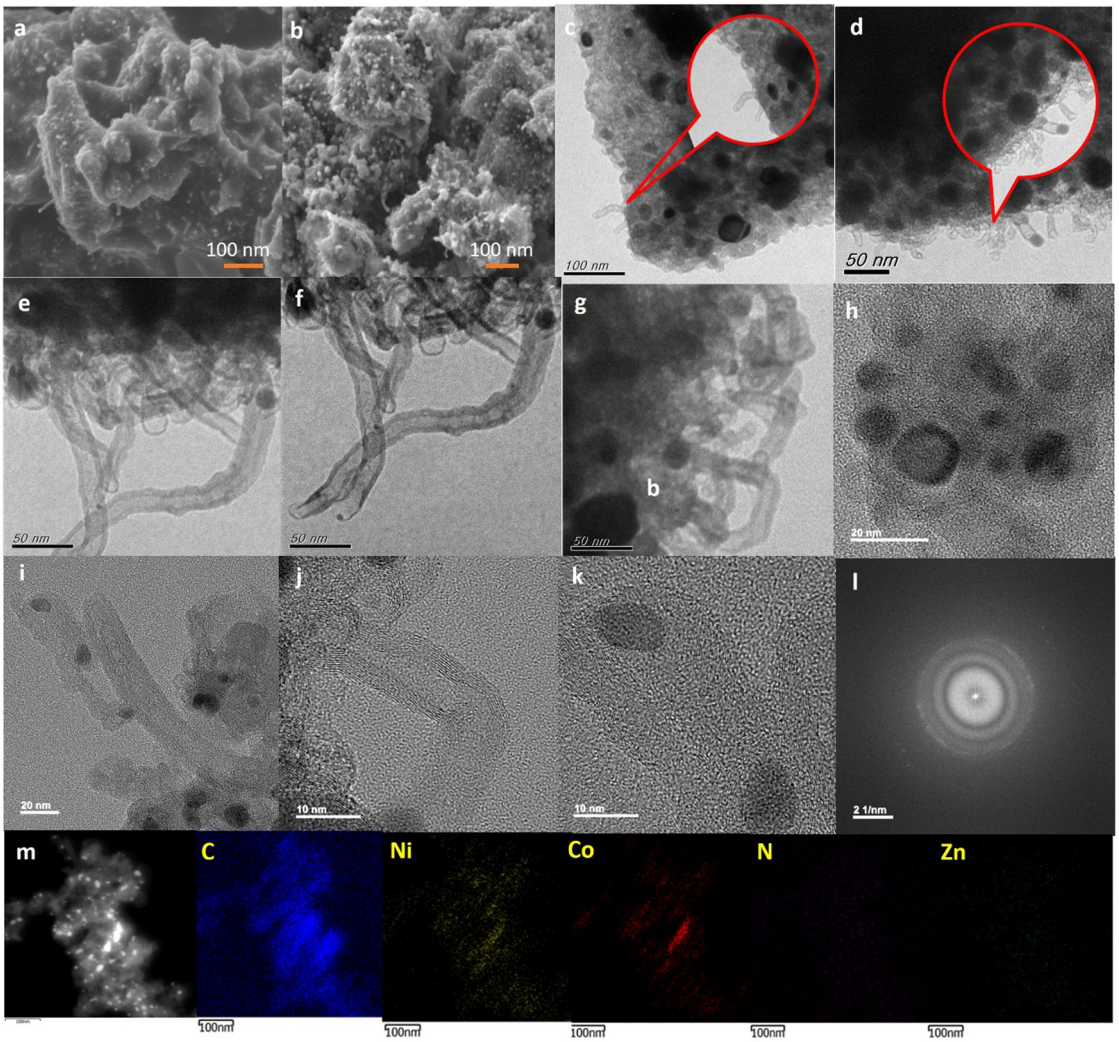

Fig. 3 FE-SEM micrograph of C-ZIF-700 (a) and C-ZIF-800 (b). TEM images of C-ZIF-700 (c) and (d). C-ZIF-800 with corresponding 50 nm scale bars showing the longer tube-like structure with multiple walls (e)–(g) with long multiwalled tube-like architecture with encapsulated Ni and Co nanoparticles in the metallic phase. A clear view of encapsulated Ni and Co nanoparticles (h). Encapsulated nanoparticles in the metallic phase (Ni, Co) in C-ZIF-800-NC show a longer multi-walled tube-like morphology holding active metal nanoparticles (i)–(k). HR-TEM showing the crystal lattice of C-ZIF-800 with *d*-spacings 0.21 nm (Ni) (111) and 0.32 nm (N–C) and corresponding FFT image (marked grey region) (l). HAADF-STEM electron image of C-ZIF-800 (m) and corresponding C, N, Ni, Co, Zn elemental maps showing the predominance of Ni metallic nanoparticles.

capacitance. The encapsulation of Ni and Co centers is predominantly shown in Fig. 3(g) and (h), in which metal nanoparticles are located within the nanotube extensions. The encapsulation of metal centers is further shown in Fig. 3(i), followed by Fig. 3(j), in which the multiwalled architecture of MWCNT is evident. The walls of these tubes are clear as uniform distances are maintained by the several layers. Fig. 3(k) shows that the MWCNT-like tubes hold multiple metal sites encapsulated in a tube-like architecture. HR-TEM of C-ZIF-800 nanoparticles and corresponding fast Fourier transform (FFT) reveal *d*-spacings of 0.21 nm for Ni (111) and Co (200), and 0.32 nm for (N–C) (Fig. 3(l)). FFT images, generated from the sample analysis, provide diffraction patterns in reciprocal space of the selected region of the HR-TEM image. The high-angle annular dark-field scanning transmission electron microscopy (HAADF-STEM) electron image of C-ZIF-800 Fig. 3(m) and corresponding C, N, Ni, Co, Zn elemental maps show the predominance of Ni-sites in the nanotube architecture. We determined the average crystallite size of Ni, Co nanoparticles as 11.2 nm (Fig. S6, ESI†), whereas the crystallite size (*D*) of Ni, Co nanoparticles obtained from the XRD peaks (Fig. 1(a) and Equation 8, ESI†) is 7.0 nm, which is slightly smaller than the particle size observed from the TEM image. Such a variation in the crystallite size (*D*) with TEM particle size was noticed in the case of CeO_2.[36]

Electrochemical measurement

Three-electrode test

For preliminary analysis of the supercapacitance properties, three-electrode electrochemical measurement was carried out using catalyst-modified glassy carbon (GC), Ag/AgCl in 3 M

© 2023 The Author(s). Published by the Royal Society of Chemistry

Open Access Article. Published on 10 agosto 2023. Downloaded on 28/07/2025 11:14:35.
This article is licensed under a Creative Commons Attribution 3.0 Unported Licence.

saturated KCl solution, and platinum wire as the working, reference, and counter electrode, respectively. The energy storage performance of the as-prepared trimetallic (Ni, Co, Zn) M-ZIF, C-ZIF-700 and C-ZIF-800 was studied by taking 1 M KOH as the electrolyte. The activity of the M-ZIF electrode towards supercapacitance is optimized by varying the temperature, *i.e.*, 700 °C and 800 °C and Co ratio. The supercapacitive performance of the C-ZIF-800 electrode is compared with M-ZIF and C-ZIF-700 at a sweep rate of 100 mV s^{-1} (Fig. S7(a), ESI†). With increasing temperature and Co ratio, the area of the cyclic voltammetry (CV) curve increases. Therefore, C-ZIF-800 is considered the standard electrode material for all electrochemical measurements. The area of the CV curve of the C-ZIF-800 hybrid electrode is much higher than those of M-ZIF and C-ZIF-700, which indicates higher capacitive behaviour. A well-defined pair of redox peaks characteristic of pseudocapacitor behaviour can be observed for all the electrode materials. It can be observed from the CV curve that the current values for oxidation and reduction peaks are augmented with an increase in sweep rates; this signifies that the charge-storage processes are of the diffusion control type. However, with an increase in the sweep rate, the oxidation and reduction peak potentials are slightly displaced towards higher and lower potentials, respectively. This may be due to the strengthened electric polarization and the possible kinetic irreversibility at the electrode and electrolyte interface. The CV plots of C-ZIF-800, C-ZIF-700, and M-ZIF at different scan rates are presented in Fig. S7(b)–(d) (ESI†). The galvanostatic charge–discharge (GCD) curve of the C-ZIF-800 electrode is much slower and nonlinear, which indicates outstanding Coulombic efficiency and good reversibility. This nonlinear discharge curve with an obvious discharge plateau is the characteristic feature of a pseudocapacitor-type electrode, which further demonstrates that the charge–discharge mechanism follows the faradaic process. C-ZIF-800 achieves a capacitance value of 849.47 F g^{-1} at 1 A g^{-1}, which is higher than those of C-ZIF-700 (198.27 F g^{-1}) and M-ZIF (190.18 F g^{-1}) (Fig. S8, ESI†). The GCD plots of C-ZIF-800, C-ZIF-700, and M-ZIF at different current densities are presented in Fig. S9(a)–(c) (ESI†). As depicted in the electrochemical impedance spectra (EIS) in Fig. S10 (ESI†), The C-ZIF-800 electrode exhibits a reduced iR-drop, indicating greater conductivity and a quicker *I–V* response. The EIS curves of M-ZIF, C-ZIF-700, and C-ZIF-800 were recorded in the frequency domains of 0.1 Hz and 100 kHz. The C-ZIF-800 catalyst possesses smaller R_s and R_{ct} values than other electrode materials, suggesting higher electrochemical performance. The cyclability test of the C-ZIF-800 electrode exhibits long-term durability with capacitance retention of more than 100% after 5000 cycles, as shown in Fig. S11 (ESI†).

To explore the detailed energy storage mechanism of as-prepared C-ZIF-800, the individual percentages of the diffusion-controlled contribution and surface-capacitive contribution were evaluated. The correlation between the scan rate and current from CV is represented using a power law in eqn (1):

$$I = a\nu^b \quad (1)$$

where I is the peak current, ν represents the sweep rate, and a and b are constants. The b-value indicates the degree of diffusion-controlled and surface-capacitive processes, which can be evaluated from the slope of a plot of $\log[I]$ *vs.* $\log[\nu]$, as shown in (Fig. 4(a)). The value of b is either 0.5 or 1, which indicates whether it is of diffusion-controlled or surface-capacitive type. The mechanism of charge storage follows the faradaic process through a surface-capacitive process, which is confirmed by the computed b-value of 0.87 from Fig. 4(a).

To obtain the approximate percentage of the contribution, eqn (2) was taken into account:

$$I = k_1\nu + k_2\nu^{1/2} \quad (2)$$

here $k_1\nu$ and $k_2\nu^{1/2}$ are the contributions of current from the surface-capacitive and diffusion-controlled processes, respectively. The k_1 and k_2 values can be extracted from the slope and intercept. The corresponding slopes and intercepts are calculated from a linear fit of the $i/\nu^{1/2}$ *vs.* $\nu^{1/2}$ plot in Fig. 4(b). Fig. 4(c) presents the percentage of surface-capacitive contribution and diffusion-controlled contribution out of the overall capacitance of as-prepared C-ZIF-800 at 40 mV s^{-1}. Fig. 4(d) shows that at a lower scan rate, the diffusion-controlled contributions dominate over the surface-capacitive contribution at 82% and gradually decrease to 45%, suggesting the charge storage mechanism follows the faradaic process through a surface-capacitive process.

Asymmetric supercapacitors

To investigate the performance of a two-electrode coin cell device, an asymmetric supercapacitor (ASC) device was built utilizing C-ZIF-800 as the positive electrode and activated carbon (AC) as the negative electrode in 1 M KOH aqueous electrolyte (CR2032).

To construct the ASC device, a three-electrode electrochemical investigation analyzing the CV for AC was undertaken (Fig. 5(a)). Fig. 5(b) depicts the CV graphs of the C-ZIF-800 and AC electrodes in various potential windows at a sweep rate of 100 mV s^{-1} in three-electrode setups. Charge equilibrium was maintained for the two-electrode device by adjusting the mass loading of the active materials in accordance with eqn (S7) (ESI†). The optimization of the potential window for this ASC was performed in the potential range of 0–1.7 V (Fig. 5(c)). The CV curve has a nice quasi-rectangular shape between 0 and 1.7 V; hence, the 0–1.7 V potential window was maintained as the optimal potential window for further research into the device. Fig. 5(d) illustrates the CV curves of the ASC device at different scan speeds (1–1000 mV s^{-1}). Fig. 5(e) depicts the GCD curves at several potentials ranging from 1.0 V to 1.7 V. To determine the capacitance value and specific capacity of the ASC device, a GCD analysis was undertaken at several current densities (Fig. 5(f)). The specific capacity was found 599.7, 544.1, 529.1, 499.4, 456.0, 392.8, and 347 C g^{-1} at the current density of 0.25, 0.5, 1, 2, 3, 4, and 5 A g^{-1}, respectively (Fig. 5(g)). As shown in Fig. 5(g), the ASC device has a maximum specific capacity of 599.7 C g^{-1} at 0.25 A g^{-1}, and the capacity value was maintained at 57.8%

Open Access Article. Published on 10 agosto 2023. Downloaded on 28/07/2025 11:14:35.
This article is licensed under a Creative Commons Attribution 3.0 Unported Licence.

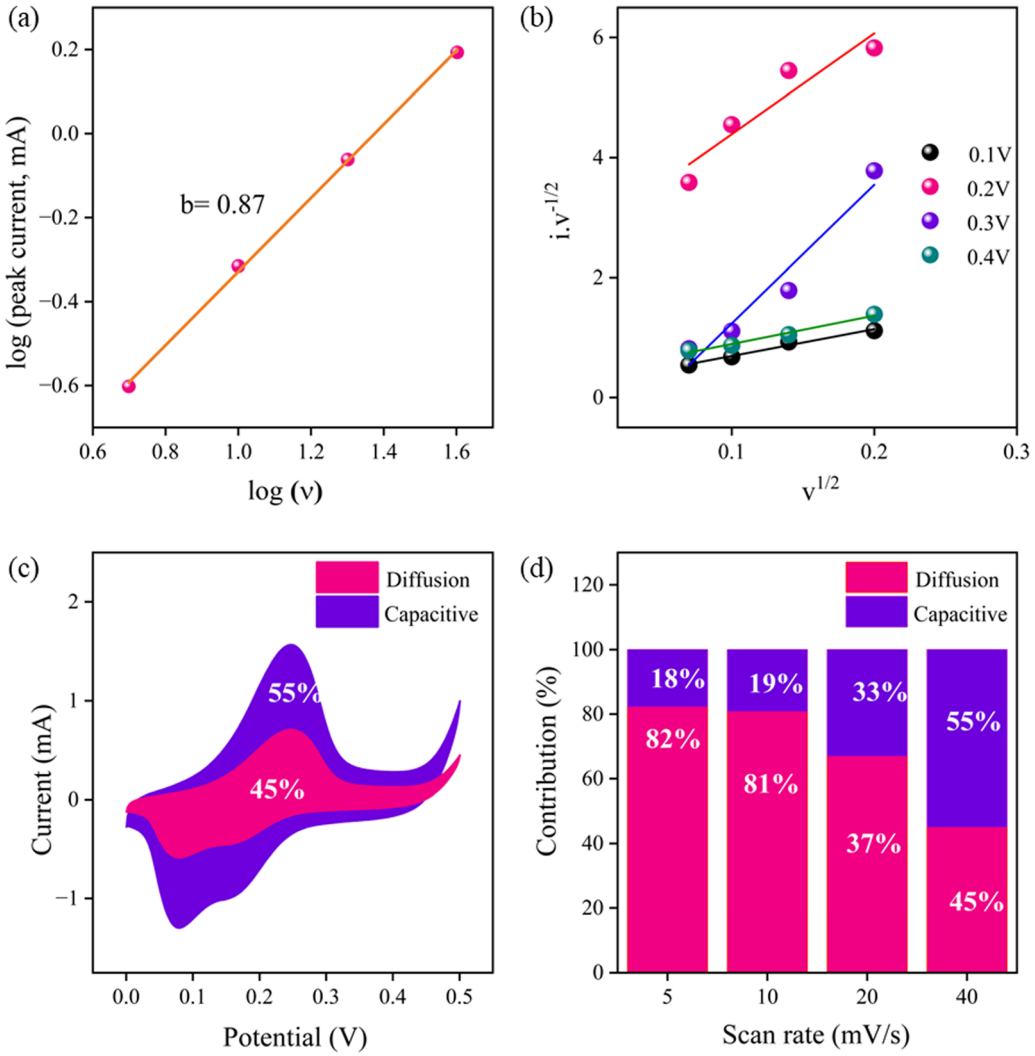

Fig. 4 (a) log(*ν*) *vs.* log(peak current) profile for finding the *b*-value. (b) $i/\nu^{1/2}$ *vs.* $\nu^{1/2}$ profile. (c) Percentage contribution of surface capacitance and diffusion-controlled capacitance for C-ZIF-800 in 1 M KOH electrolyte at 40 mV s^{-1}. (d) Bar diagram representing percentage contributions at various scan rates.

even after 5 A g^{-1} (370 C g^{-1}). In addition, the ASC device provides an outstanding energy density of 141.59 W h kg^{-1} at a power density of 212.5 W kg^{-1}, while retaining 81.93 W h kg^{-1} at a power density of 4250 W kg^{-1} (Fig. 5(h)). Table S1 (ESI†) provides a more extensive assessment of the published literature using a conventional two-electrode device. Due to the porosity network, the ASC device (C-ZIF-800/AC) has demonstrated excellent electrochemical performance. Fig. 5(i) depicts the electrochemical impedance spectroscopy (EIS) investigation conducted to determine the kinetic behavior of the as-prepared composites. The ASC exhibits a very low R_s of 7.62 and a minimum R_{ct} of 0.72, which substantiates its exceptional electrical conductivity. Two ASCs were manufactured and the device was charged at a current density of 1 A g^{-1} using an electrochemical workstation in order to examine its practical capabilities further. The two ASCs were linked in series to illuminate a 1.5 V LED with great brightness at the time of illumination, indicating substantial storage capacity (Fig. 5(j)–(l)).

The combination of HRTEM, XPS, and EXAFS techniques supports the presence of Ni and Co centers in encapsulated form in N–C nanotubes in C-ZIF-800. The multimetallic design with the maximized number of favorable active sites offered may have optimized the electronic structure of the C-ZIF-800 electrode.

In the given case studies, Ni–Mn LDH/rGO/$Ni(OH)_2$@Ni foam exhibits high-performance capacitance with a specific energy density of 0.23 mW h cm^2 at a specific power density of 0.91 mW cm^2.[37] Nickel-nanoparticle-modified MnO nanosheet arrays wherein Ni NPs promote the accumulation and release of electrons at the interface of Ni/MnO, which contributes extra capacitance to the composite, are similar to the case of C-ZIF-800 with porous electrochemically exposed active sites.[38] An asymmetric supercapacitor of $Ni(OH)_2$/A/CNT in 6 M KOH within a 1.6 V window offers a maximum specific capacitance of 82.1 F g^{-1} with an energy density of 32.3 W h kg^{-1} at a power density of 504.8 W kg^{-1}.[39] The hierarchical structure in the

© 2023 The Author(s). Published by the Royal Society of Chemistry

Open Access Article. Published on 10 agosto 2023. Downloaded on 28/07/2025 11:14:35.
This article is licensed under a Creative Commons Attribution 3.0 Unported Licence.

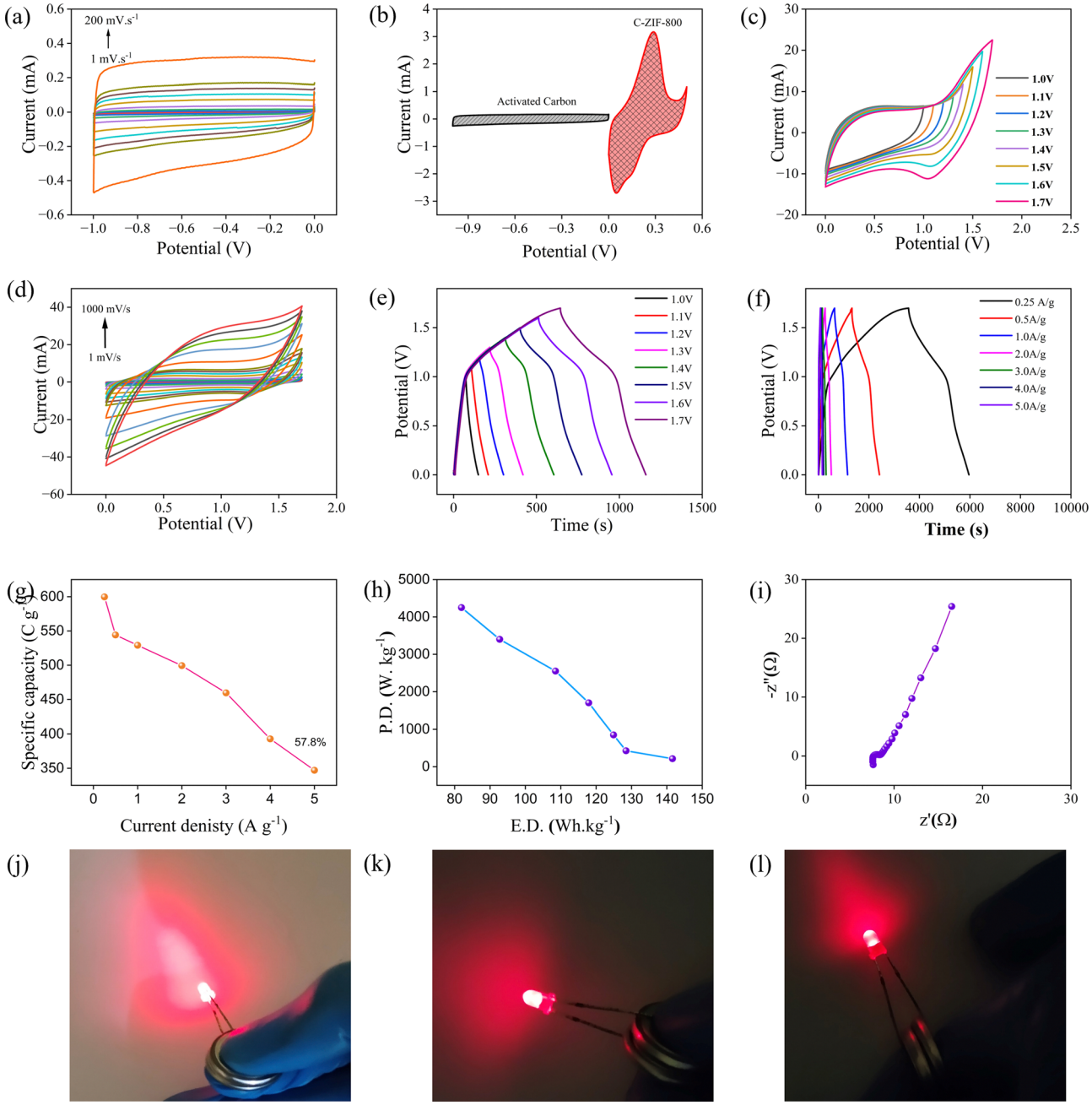

Fig. 5 Electrochemical measurements of the ASC device (activated carbon (AC)//C-ZIF-800). (a) CV plots of activated carbon at different scan rates from 1 to 200 mV s^{-1}. (b) CV plots of individual activated carbon and C-ZIF-800 at 100 mV s^{-1} scan rate. (c) CV profiles of the ASC at different step potentials. (d) CV plots of the ASC at various scan rates. (e) Specific capacitance as a function of scan rate. (f) Stepped GCD profile at a fixed current density. (g) GCD plot at different current densities from 0.25 A g^{-1} to 5 A g^{-1}. (h) Ragone pot of the as-fabricated ASC device. (i) Electrochemical impedance spectroscopy (EIS) plot of the fabricated device. (j)–(l) Photographs of the lighting of a red LED by connecting two ASC devices in series.

combination of Ni and Ag nanoparticles on rGO offers a synergistic effect and retention of capacitance with supercapacitive performance.[40,41] Our studies of several faradaic capacitance materials, such as Mn_3O_4 in a graphene matrix and MoS_2-rGO, showed both experimental and theoretical insights into the origin of capacitance enhancement and storage.[18,42,43] In Table S1 (ESI†), we have listed a series of Ni-centered MOF and CNT-based capacitance with specific capacitance, power density, and energy density, including capacitance retention cycle number to represent cyclic stability. The trend in specific capacitance suggests that C-ZIF-800 offers a unique morphology along with the key role of Ni metallic sites offering a synergistic effect of bimetallic (Ni and Co) interface on the multi-walled CNT of C-ZIF-800. The effect of Ni-O and Ni nanoparticles in the metallic valence state in a multimetallic design has not been extensively studied, so this report focuses on enhancing capacitance and the fabrication of an asymmetric supercapacitor. The enhanced capacitance of C-ZIF-800 was

Open Access Article. Published on 10 agosto 2023. Downloaded on 28/07/2025 11:14:35.
This article is licensed under a Creative Commons Attribution 3.0 Unported Licence.

compared with other relevant Ni-centred electrodes, which suggests that Ni-metal sites with cobalt NPs and a conductive tube-like network in the N–C facilitate enhanced capacitance. In the case studies given in Table S1 (ESI†), in terms of capacitance electrode performance, the energy density and capacitance retention of C-ZIF-800 are far ahead, and it is perhaps successful as a result of the nanotube-like architecture with predominant Ni, Co sites along with a multimetallic design. An asymmetric supercapacitor based on bimetallic nanoparticles of Ni and Co on micro–meso carbon utilizes the synergistic effect between the bimetallic sites and support materials[44] consisting of a hierarchical porous and unique nanoarchitecture, as in the case of C-ZIF-800 with a multi-walled nanotube network. The synergistic effect between Ni–Co bimetallic sites with a hierarchical porous support and unique tube-like morphology enables facile electron/ion transfer in the electrolyte, resulting in performance over an enlarged voltage window for powering an LED device for several minutes. Not only the bimetallic synergistic effect but also Ni-Co bimetallic sites offer rich sites for redox reactions with internal ultrahigh conductivity for faster electron transfer with an average thickness of electrode.[45] In this work, Table S1 (ESI†) includes the electrochemical performance of C-ZIF-800 in three electrodes being retained for 5000 cycles. Therefore, the combined role of Ni–Co bimetallic sites with abundant pores for synergism between electron transfer events and protection of metallic centers in tubular encapsulation is considered to be responsible for the enhanced capacitance retention.

A connection between the MWCNT and double-layer capacitance can be assumed based on the experimental results for electrochemical impedance and capacitance. Such bimetallic C-ZIF-800 with CNT-type tubular architecture of N–C favors the electrical double-layer (EDL) mechanism of charge transfer, but the presence of predominant Ni metal nanoparticles and possible Ni–O bonding favors the faradaic mechanism of charge transfer.[46] The smaller iR-drop of C-ZIF-800 suggests higher conductivity and rapid *I–V* response, as confirmed by the impedance spectra (Fig. 5(i)). Moreover, Ni 2p and Co 2p XPS spectral patterns confirm the formation of Ni(II)/Ni–O and Co metallic sites, which favors the faradaic pseudocapacitance mechanism for high charge storage. Based on the EIS and XPS observations, the charge storage mechanism depends on polarization, wherein counter-ion adsorption and co-ion desorption are key routes to ion-exchange. Pure counterion-adsorption in the positive electrode and excess ionic charge in the pores of C-ZIF-800 would balance the electronic charge in both electrodes.

Table S1 (ESI†) includes the energy density, power density of C-ZIF-800 as an ASC and cyclic stability in three-electrode measurements, the capacitance retention for 5000 cycles was witnessed. A valid comparison of our current findings with other relevant reports revealing the combined role of Ni–Co bimetallic sites along with single Ni or Co metal sites with abundant pores is included in Table S1 (ESI†). Abundant pores for synergism between electron transfer event and protection of metallic sites in a tubular structure that encapsulates the metals is considered to be responsible for the difference in enhanced capacitance retention. When comparing the capacitance retention percentage, a performance range of 80 of 90% was noted for most NiCo bimetallic capacitors.

Conclusions

In summary, a nanotube with multi-wall supports encapsulating Ni and Co in a metallic valence state was fabricated *via* the high-temperature pyrolysis of a trimetallic MOF in a porous graphene-like multi-walled N–C matrix. The porous N–C matrix offers adequate exposure to metallic sites, enabling effective modulation of the electronic structures of the metal centers. The rich electronics of Co and Ni-sites on the N–C matrix were confirmed using XPS, XAS, and HR-TEM techniques. Among the configurations, the graphitic N-decorated Ni and Co metallic sites enabled them to act as faradaic electrodes for longer-term charge–discharge stability than many reported materials, as shown in Table S1 (ESI†). Higher discharge power density, high capacitance, and better long-term stability compared to commercial Pt/C + Ru_2O enable our strategy to provide highly active materials for capacitance-based charge storage. Finally, an ASC device (C-ZIF-800//AC) with a wide potential window of 1.7 V was successfully fabricated. The device offers an excellent specific capacity of 599.7 C g^{-1} at 0.25 A g^{-1} with an exceptional energy density of 141.59 W h kg^{-1} at a power density of 212.5 W kg^{-1}, retaining 81.93 W h kg^{-1} at a power density of 4250 W kg^{-1}. The as-fabricated device demonstrated its potential for future energy storage applications by illuminating a red LED light for 60 min by combining two devices in series. The novelty of the current work originates from the strategy of deriving a Ni–Co system with predominantly Ni centers on C-ZIF-800 encapsulated in a nanotube architecture, which was explored for ASC and LED studies.

Conflicts of interest

Authors have no conflict of interest to declare.

Acknowledgements

SD wishes to acknowledge research funding support by the Department of Biotechnology, Ministry of Science & Technology, Government of India for the grant number BT/RLF/Re-entry/41/2017 under DBT Ramalingaswami Re-entry Fellowship (2019-2024) and DBT-Energybioscience-Biofuels research grant (2022-2025 BT/PR38594/PBD/26/795/2020). B. K. J. acknowledges CSIR (HCP-42; OLP-48), NALCO, BRNS, MNRE, India for financial support. OA wishes to acknowledge the UGC-DAE-CSR Government of India and Smt. Babita Vinayak Salaskar from Beamline Development and application section, BARC for EXAFS measurements. KCW is thankful to the National Science and Technology Council (NSTC), Taiwan (111-2124-M-002-021 and 111-2628-E-002-008) for the funding support. Also, financial support by the Center of Atomic Initiative for New Materials, National Taiwan University, from the Featured Areas Research Center Program within

© 2023 The Author(s). Published by the Royal Society of Chemistry

Open Access Article. Published on 10 agosto 2023. Downloaded on 28/07/2025 11:14:35.
This article is licensed under a Creative Commons Attribution 3.0 Unported Licence.

the framework of the Higher Education Sprout Project by the Ministry of Education in Taiwan (111L900801), is acknowledged.

References

1 J. Huang, K. Yuan and Y. Chen, *Adv. Funct. Mater.*, 2022, **32**, 2108107.
2 S. K. Das, L. Pradhan, B. K. Jena and S. Basu, *Carbon*, 2023, **201**, 49–59.
3 E. Zhang, N. Fulik, G.-P. Hao, H.-Y. Zhang, K. Kaneko, L. Borchardt, E. Brunner and S. Kaskel, *Angew. Chem., Int. Ed.*, 2019, **58**, 13060–13065.
4 Y. Shao, M. F. El-Kady, J. Sun, Y. Li, Q. Zhang, M. Zhu, H. Wang, B. Dunn and R. B. Kaner, *Chem. Rev.*, 2018, **118**, 9233–9280.
5 D. Lee, S. Mathur and K. H. Kim, *Nano Energy*, 2021, **86**, 106076.
6 S. Ding, J. An, D. Ding, Y. Zou and L. Zhao, *Chem. Eng. J.*, 2022, **431**, 134100.
7 G. Wang, Z. Yan, N. Wang, M. Xiang and Z. Xu, *ACS Appl. Nano Mater.*, 2021, **4**, 9034–9043.
8 J. Balamurugan, T. T. Nguyen, V. Aravindan, N. H. Kim and J. H. Lee, *Adv. Funct. Mater.*, 2018, **28**, 1804663.
9 S. Zhang, M. Zheng, Y. Tang, R. Zang, X. Zhang, X. Huang, Y. Chen, Y. Yamauchi, S. Kaskel and H. Pang, *Adv. Funct. Mater.*, 2022, **32**, 2204714.
10 R. Patil, S. Liu, A. Yadav, N. Khaorapapong, Y. Yamauchi and S. Dutta, *Small*, 2022, **18**, 2203147.
11 V. Šedajová, A. Bakandritsos, P. Błoński, M. Medveď, R. Langer, D. Zaoralová, J. Ugolotti, J. Dzíbelová, P. Jakubec, V. Kupka and M. Otyepka, *Energy Environ. Sci.*, 2022, **15**, 740–748.
12 T. S. Mathis, N. Kurra, X. Wang, D. Pinto, P. Simon and Y. Gogotsi, *Adv. Energy Mater.*, 2019, **9**, 1902007.
13 S. Fleischmann, Y. Zhang, X. Wang, P. T. Cummings, J. Wu, P. Simon, Y. Gogotsi, V. Presser and V. Augustyn, *Nat. Energy*, 2022, **7**, 222–228.
14 J. Zhao, B. Wu, X. Huang, Y. Sun, Z. Zhao, M. Ye and X. Wen, *Adv. Sci.*, 2022, **9**, 2201678.
15 S. Boyd, K. Ganeshan, W.-Y. Tsai, T. Wu, S. Saeed, D.-E. Jiang, N. Balke, A. C. T. van Duin and V. Augustyn, *Nat. Mater.*, 2021, **20**, 1689–1694.
16 L. Liu, Z. Xie, X. Du, D. Yu, B. Yang, B. Li and X. Liu, *Chem. Eng. J.*, 2022, **430**, 132815.
17 L. Pradhan, B. Nayak, A. Mukherjee, S. Basu, P. Bhanja and B. K. Jena, *ACS Appl. Energy Mater.*, 2023, **6**, 3347–3356.
18 S. K. Das, S. Kamila, B. Satpati, M. Kandasamy, B. Chakraborty, S. Basu and B. K. Jena, *J. Power Sources*, 2020, **471**, 228465.
19 B. Mohanty, L. Giri and B. K. Jena, *Energy Fuels*, 2021, **35**, 14304–14324.
20 L. Xu, W. Zhou, S. Chao, Y. Liang, X. Zhao, C. Liu and J. Xu, *Adv. Energy Mater.*, 2022, **12**, 2200101.
21 H. Ma, H. Chen, Y. Hu, B. Yang, J. Feng, Y. Xu, Y. Sun, H. Cheng, C. Li, X. Yan and L. Qu, *Energy Environ. Sci.*, 2022, **15**, 1131–1143.
22 Y. Chen, H. Hou, B. Liu, M. Li, L. Chen, C. Chen, S. Wang, Y. Li and D. Min, *Chem. Eng. J.*, 2023, **454**, 140453.
23 X. Hong, C. Deng, G. Wang, X. Wang and W. Dong, *Chem. Eng. J.*, 2023, **451**, 139036.
24 F. Shi, S. Zhao, J. Yang, Y. Tong, J. Li, S. Zhai, X. Zhao, S. Wu, H. Li, Q. An and K. Wang, *J. Mater. Chem. A*, 2022, **10**, 12679–12691.
25 S. J. Marje, S. S. Pujari, S. A. Khalate, V. V. Patil, V. G. Parale, T. Kim, H.-H. Park, J. L. Gunjakar, C. D. Lokhande and U. M. Patil, *J. Mater. Chem. A*, 2022, **10**, 11225–11237.
26 K. Li, X. Liu, T. Zheng, D. Jiang, Z. Zhou, C. Liu, X. Zhang, Y. Zhang and D. Losic, *Chem. Eng. J.*, 2019, **370**, 136–147.
27 K. Li, S. Feng, C. Jing, Y. Chen, X. Liu, Y. Zhang and L. Zhou, *Chem. Commun.*, 2019, **55**, 13773–13776.
28 K. Li, Z. Guo, Q. Sun, X. Dai, Y. Li, K. Yao, X. Liu, Z. Bao, J. Rao and Y. Zhang, *Chem. Eng. J.*, 2023, **454**, 140223.
29 K. Li, Y. Xiao, T. Zheng, Q. Sun, Y. Zhang, H. Teng, W. Wang, K. Yao, J. Rao and Y. Zhang, *Appl. Surf. Sci.*, 2023, **622**, 156950.
30 T. Munawar, M. Shahid Nadeem, F. Mukhtar, S. Manzoor, M. Naeem Ashiq and F. Iqbal, *Mater. Sci. Eng., B*, 2022, **284**, 115900.
31 M. Naveed Ur Rehman, T. Munawar, M. S. Nadeem, F. Mukhtar, U. A. Akbar, S. Manzoor, A. S. Hakeem, M. N. Ashiq and F. Iqbal, *Solid State Sci.*, 2022, **128**, 106883.
32 T. Munawar, F. Mukhtar, M. S. Nadeem, S. Manzoor, M. N. Ashiq, M. Riaz, S. Batool, M. Hasan and F. Iqbal, *Ceram. Int.*, 2022, **48**, 19150–19165.
33 B. Ding, Z. Fan, Q. Lin, J. Wang, Z. Chang, T. Li, J. Henzie, J. Kim, H. Dou and X. Zhang, *Small Methods*, 2019, **3**, 1900277.
34 R. Patil, N. Kumar, S. Bhattacharjee, H.-Y. Wu, P.-C. Han, B. M. Matsagar, K. C. W. Wu, R. R. Salunkhe, A. Bhaumik and S. Dutta, *Chem. Eng. J.*, 2023, **453**, 139874.
35 W. Liu, C. Lu, X. Wang, K. Liang and B. K. Tay, *J. Mater. Chem. A*, 2015, **3**, 624–633.
36 T. Munawar, A. Bashir, M. S. Nadeem, F. Mukhtar, S. Manzoor, M. N. Ashiq, S. A. Khan, M. Koc and F. Iqbal, *Ceram. Int.*, 2023, **49**, 8447–8462.
37 Y. Lin, S. Su, H. Dai, X. Xiang, P. Li and X. Zhu, *J. Energy Storage*, 2022, **56**, 106138.
38 M. Huang, Y. Lin, H. Huang, X. Fan, K. Shi, Z. Yang and W. Zhang, *Electrochim. Acta*, 2021, **383**, 138353.
39 L. Sui, S. Tang, Y. Chen, Z. Dai, H. Huangfu, Z. Zhu, X. Qin, Y. Deng and G. M. Haarberg, *Electrochim. Acta*, 2015, **182**, 1159–1165.
40 M. Chandel, P. Makkar and N. N. Ghosh, *ACS Appl. Electron. Mater.*, 2019, **1**, 1215–1224.
41 W. Li, L. Xin, X. Xu, Q. Liu, M. Zhang, S. Ding, M. Zhao and X. Lou, *Sci. Rep.*, 2015, **5**, 9277.
42 S. Kamila, B. Chakraborty, S. Basu and B. K. Jena, *J. Phys. Chem. C*, 2019, **123**, 24280–24288.
43 S. Kamila, B. Mohanty, A. K. Samantara, P. Guha, A. Ghosh, B. Jena, P. V. Satyam, B. K. Mishra and B. K. Jena, *Sci. Rep.*, 2017, **7**, 8378.
44 Y. Zhang, Y. Zhang, Y. Zhang, H. Si and L. Sun, *Nano-Micro Lett.*, 2019, **11**, 35.
45 Q. Yang, Y. Liu, M. Yan, Y. Lei and W. Shi, *Chem. Eng. J.*, 2019, **370**, 666–676.
46 A. C. Forse, C. Merlet, J. M. Griffin and C. P. Grey, *J. Am. Chem. Soc.*, 2016, **138**, 5731–5744.

© 2023 The Author(s). Published by the Royal Society of Chemistry